

1 **Internal Oscillations of Tropical Mesoscale Convective Disturbances**

2 Bolei Yang^{1,2}, William R. Boos^{2,3}, Ji Nie^{1,4} and Zhe-Min Tan⁵

3
4 1. Laboratory for Climate and Ocean-Atmosphere Studies, Department of Atmospheric
5 and Oceanic Sciences, School of Physics, Peking University, Beijing, China

6 2. Department of Earth and Planetary Science, University of California, Berkeley,
7 Berkeley, California

8 3. Climate and Ecosystem Sciences Division, Lawrence Berkeley National Laboratory,
9 Berkeley, California

10 4. China Meteorological Administration Tornado Key Laboratory, Foshan, China

11 5. Key Laboratory for Mesoscale Severe Weather, School of Atmospheric Sciences,
12 Nanjing University, Nanjing, China

13
14
15
16
17 Corresponding author: Ji Nie

18 Email: nieji1984@gmail.com

19
20 Bolei Yang: blyang@pku.edu.cn

21 William R. Boos: William.boos@berkeley.edu

22 Zhe-Min Tan: zmtan@nju.edu.cn

23 This is a non-peer reviewed paper, which has been submitted to ‘Journal of the
24 atmospheric sciences.’

26
27
28
29
30
31
32
33
34
35
36
37
38
39

Abstract

In real-world observations, long-lived tropical mesoscale convective disturbances (MCDs) often exhibit quasi-periodic variations. Previous studies suggested that these variations are mainly induced by external forcings. However, some studies showed evidence that tropical MCDs can display quasi-periodic behavior even without external forcings. In this study, a suite of idealized convection-permitting simulations is used to examine the evolution of a mesoscale atmospheric column after an initial pulse of heating. It is demonstrated that the heated column not only radiates inertia-gravity waves that perturb its environment, but itself continues to oscillate with consequences for subsequent local convection. By comparing simulations with linear wave theory, it is suggested that this oscillation is an inertia-gravity oscillation. This study indicates that convectively coupled internal oscillations may constitute a fundamental component of the life cycle of observed long-lived tropical MCDs.

40 **1. Introduction**

41 Mesoscale convective disturbances are frequently observed in Earth's tropical
42 regions. These disturbances typically encompass systems like mesoscale convective
43 systems, tropical depressions, tropical cyclones (TCs), and monsoon low-pressure
44 systems (LPSs), with sizes ranging from hundreds to thousands of kilometers. These
45 convective systems not only play a crucial role in the water and energy cycles within
46 the tropics, but also significantly impact our social and economic activities (e.g., Nesbitt
47 et al. 2000; Emanuel 2018; Houze 2018). However, the mechanisms driving the
48 evolution of these systems remain unclear.

49 In real-world observations and numerical simulations, long-lived tropical
50 mesoscale convective disturbances (MCDs) often interact with external forcings and
51 demonstrate significant periodic characteristics. A typical example is the occurrence of
52 large-scale, westward-propagating convective disturbances with periods of
53 approximately 2 days in the equatorial western Pacific (e.g., Takayabu 1994; 1996).
54 Studies indicated that this 2-day period of convection is forced by the propagation of
55 equatorial waves with wavelengths of around 2000 to 4000 km (e.g., Haertel and
56 Johnson 1998; Wheeler et al. 2000; Haertel and Kiladis 2004). Another example is the
57 diurnal cycle of convection over the tropical ocean. In the nighttime, the absence of
58 shortwave heating cools the troposphere, which fosters convection by increasing
59 relative humidity and enhancing convective instability. Conversely, convection is
60 inhibited during the daytime due to strong shortwave heating in the free-troposphere
61 (e.g., Gray and Jacobson 1977; Fingerhut 1978). This diurnal cycle of convection is
62 robust in nearly all types of tropical MCDs, particularly in those with longer lifetimes,
63 such as TCs (e.g.; Browner et al. 1977; Dunion et al. 2014; Wu et al. 2014).

64 However, in many idealized simulations without external forcing, tropical MCDs
65 also exhibit pronounced quasi-periodic variations. For instance, in many idealized TC
66 genesis simulations, which lack both the diurnal insolation cycle and lateral boundary
67 forcing, significant quasi-periodic pulses of the disturbance can often be seen (e.g.,
68 Nolan 2007; Nicholls and Montgomery 2013; Yang and Tan 2020). Some studies

69 suggested that this behavior may be a model artifact resulting from the use of doubly
70 periodic boundary conditions, wherein gravity waves can return to their source and
71 trigger new convection (e.g., Nolan, 2007). Nonetheless, in simulations with very large
72 domains or damping lateral boundary conditions, quasi-periodic variation of the TC
73 disturbances still occurs (e.g., Li et al. 2006; Nicholls 2015). Similarly, quasi-periodic
74 variations can also be seen in idealized simulations of monsoon LPSs (e.g., Diaz and
75 Boos, 2021a, b). These results suggest that the quasi-periodic behavior of tropical
76 MCDs are not solely attributable to external forcing, but may also be internally
77 generated.

78 The aim of this work is to determine whether a tropical MCD could internally
79 generate quasi-periodic behaviors and, if so, to identify the mechanisms underlying
80 those behaviors. The rest of the paper is organized as follows: Section 2 introduces the
81 simulation details. Section 3 briefly analyzes the internal quasi-periodic behavior in
82 full-physics simulations. Section 4 provides evidence for the critical role of low-level
83 buoyancy in determining the precipitation. Section 5 demonstrates that the inertia-
84 gravity oscillation is responsible for the quasi-periodic behavior of low-level buoyancy
85 and precipitation. Finally, Section 6 offers a discussion and summary.

86

87 **2. Methods**

88 In this work, we use idealized numerical simulations to investigate the internal
89 oscillations of tropical MCDs. The numerical model employed is the WRF version 4.6.0
90 (Skamarock et al., 2019). The model domain extends to an altitude of 27 km, with the
91 upper third consisting of a sponge layer (Klemp and Lilly 1978). There are 50 vertical
92 levels, with 10 levels located below 1 km height. The initial sounding is derived from
93 Jordan (1958), which is a typical tropical sounding commonly used in simulations.

94 The simulations cover a horizontal domain size of $1800 \text{ km} \times 1800 \text{ km}$, with a
95 horizontal resolution of 3 km. To rule out the effects of gravity waves propagating back
96 to their sources, the best way should be using open lateral boundary conditions so that
97 gravity waves can radiate out of the domain. However, in our preliminary simulations
98 (not shown), adopting open lateral boundary condition leads to a drastic drying of the

99 domain, with the domain-mean moisture content decreasing by 40% in the first 3 days.
 100 Therefore, we still use doubly periodic lateral boundary condition, but add a sponge
 101 layer at the lateral boundaries of the domain (e.g., Li et al., 2006). This sponge layer is
 102 180 km wide at the lateral boundaries, with the diffusion coefficient set to 1000 times
 103 the model's predicted value (1.5 order TKE closure method). The simulations maintain
 104 a fixed sea surface temperature SST of 302.15 K and a constant solar radiation of 350
 105 W m^{-2} with no diurnal cycle. The Thompson microphysics scheme (Thompson et al.,
 106 2004) and the RRTMG radiation scheme (Iacono et al. 2008) are implemented in the
 107 simulations. The boundary layer (BL) scheme is YSU, coupled with the revised Monin–
 108 Obukhov surface-layer scheme (Hong et al. 2006).

109 All simulations initiate with a moist anomaly characterized by enhanced humidity
 110 at the center of the domain. This moist anomaly has a radius of 150 km and a height of
 111 3 km (starting at the surface), with the water vapor mixing ratio inside set at 110% of
 112 the initial sounding value. We conduct three simulations with Coriolis parameter set to
 113 10^{-4} s^{-1} (CTLF10), $5 \times 10^{-5} \text{ s}^{-1}$ (CTLF05) and 0 s^{-1} (CTLF0), respectively (Table 1). All
 114 the simulations are run for 72 hours, and results are output every 2 hours. In the
 115 following analysis, we will mainly focus on the results in CTLF10, and the results in
 116 the other two experiments will be briefly compared.

117

118

Table 1 Descriptions of experiments.

Name	Description
CTLF10	An 1800 km×1800 km full-physics simulation with Coriolis parameter set to be $1 \times 10^{-4} \text{ s}^{-1}$. The lateral boundary condition is double periodic, with a damping layer of 180 km wide.
CTLF05	As CTLF10, with Coriolis parameter set to be $5 \times 10^{-5} \text{ s}^{-1}$.
CTLF0	As CTLF10, without Coriolis force.
Dry_Developing	A 3000 km×3000 km simulation forced with the heating profile averaged in the developing stage of CTLF10. There is no microphysics or radiation parameterization, and the open lateral boundary condition is used. The other settings are with CTLF10.
Dry_Decaying	As Dry_Developing, with the forcing heating profile to be that averaged in the decaying stage.
Dry2_F10	As Dry_Developing, forced with a stratiform heating profile shown in Fig. 6b.
Dry2_F05	As Dry2_F10, with Coriolis parameter set to be $5 \times 10^{-5} \text{ s}^{-1}$.

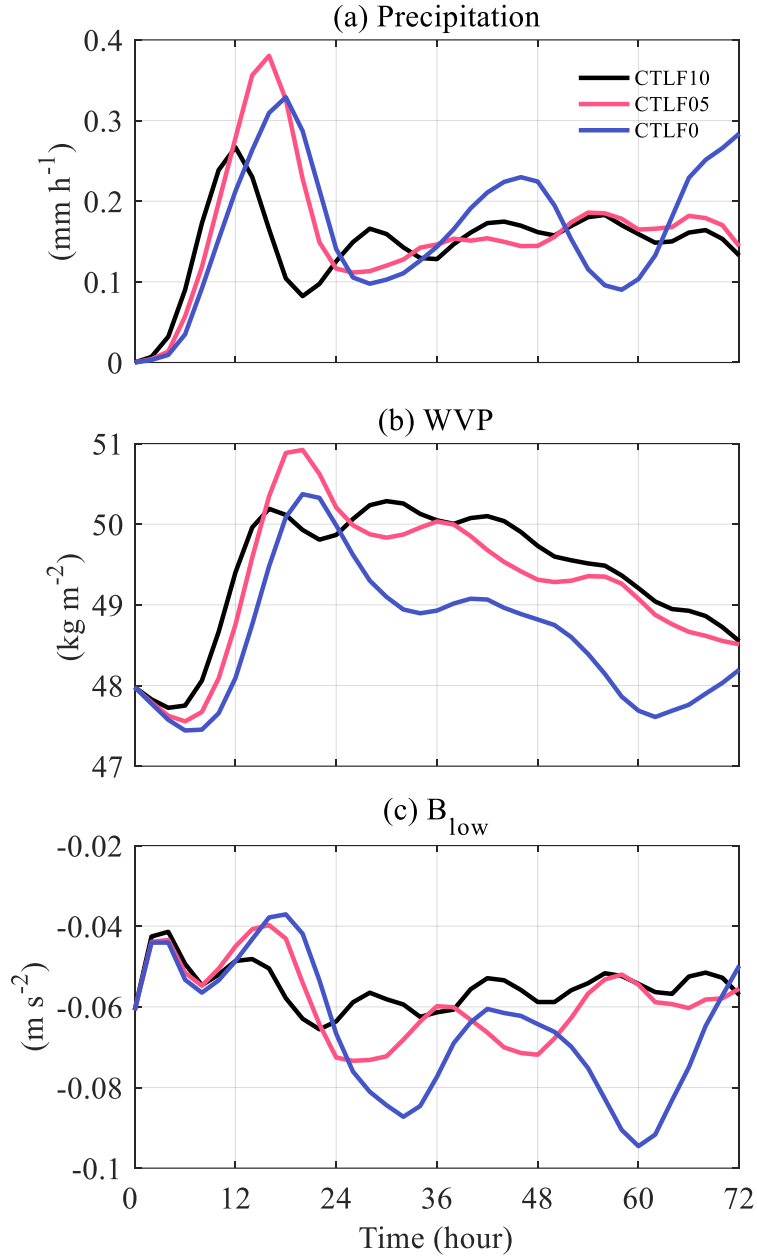
Dry2_F0	As Dry2_F10, without Coriolis forcing.
Dry1_F10	As Dry2_F10, forced with a deep convective heating profile shown in Fig. 6b.
Dry1_F05	As Dry1_F10, with Coriolis parameter set to be $5 \times 10^{-5} \text{ s}^{-1}$.
Dry1_F0	As Dry1_F10, without Coriolis force.

119

120

121 **3. Internal oscillation of tropical MCDs**

122 The time series of the precipitation rate in the disturbed region (defined to be the
123 inner 150 km radii of the disturbance) of the three simulations are shown in Fig. 1a. All
124 three simulations exhibit significant oscillations. Specifically, the periods in CTLF10,
125 CTLF05 and CTLF0 are around 15 hours, 18 hours and 28 hours (the period is defined
126 as the time lag between the first and the last precipitation peaks divided by the number
127 of cycles), respectively, indicating a noticeable increase in the period as the Coriolis
128 parameter decreases. The water vapor path (WVP) in the disturbance region also shows
129 significant oscillation, which is almost in phase with the precipitation (Fig. 1b).



130

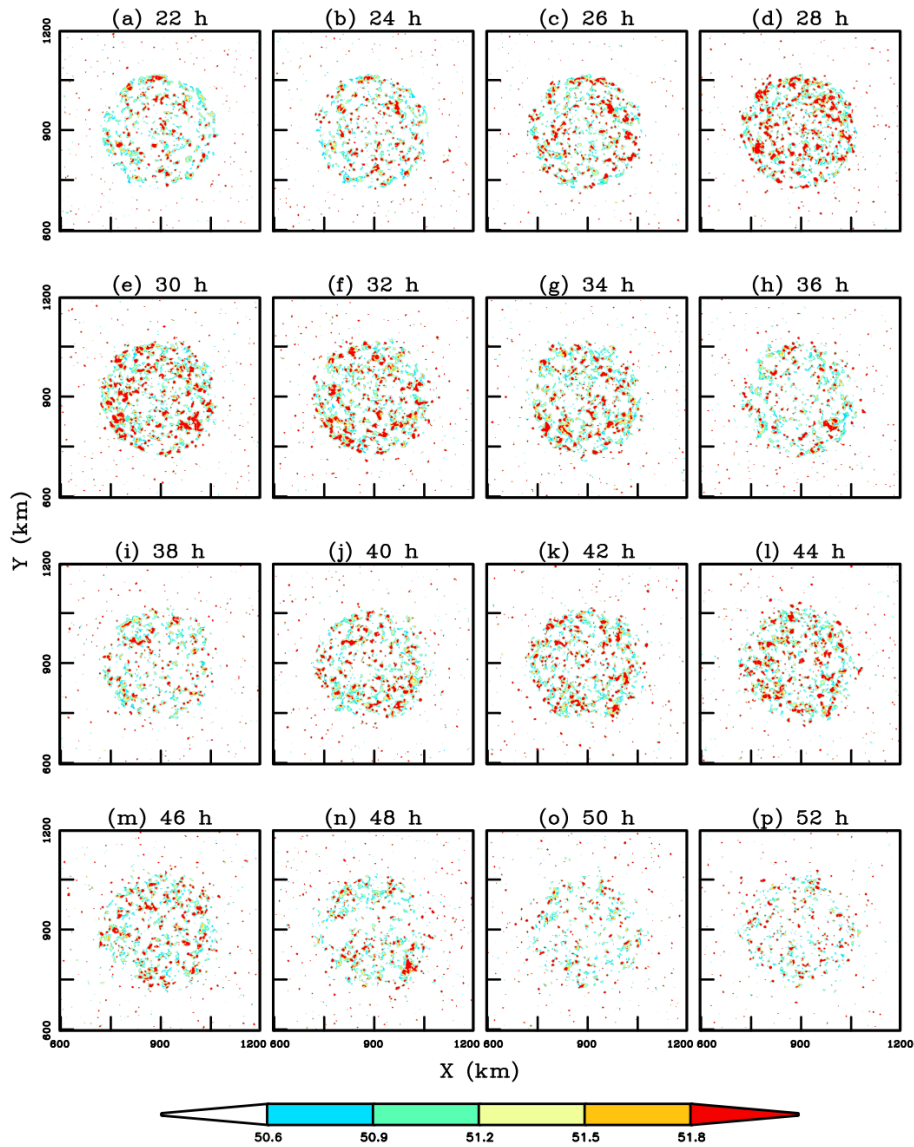
131 **Fig.1** Time series of (a) precipitation (mm h^{-1}) (b) water vapor path (kg m^{-2}) and (c)
 132 low-level buoyancy (m s^{-2}) over the inner 150 km radii of the disturbance in CTLF10
 133 (black), CTLF05 (red), and CTLF0 (blue).

134

135 To confirm that this oscillation is physically meaningful rather than a result of
 136 model noise, we first present plane views of WVP from 22 h to 52 h in CTLF10 (Fig.
 137 2). In Fig. 2, the WVP shows clear oscillations, which is mainly confined in the
 138 disturbed area. The WVP has an increasing trend from 22-28 h and 38-44 h, and a
 139 decreasing trend from 30-36h and 46-52h, consistent with the variation of WVP shown

140 in Fig. 1b.

141



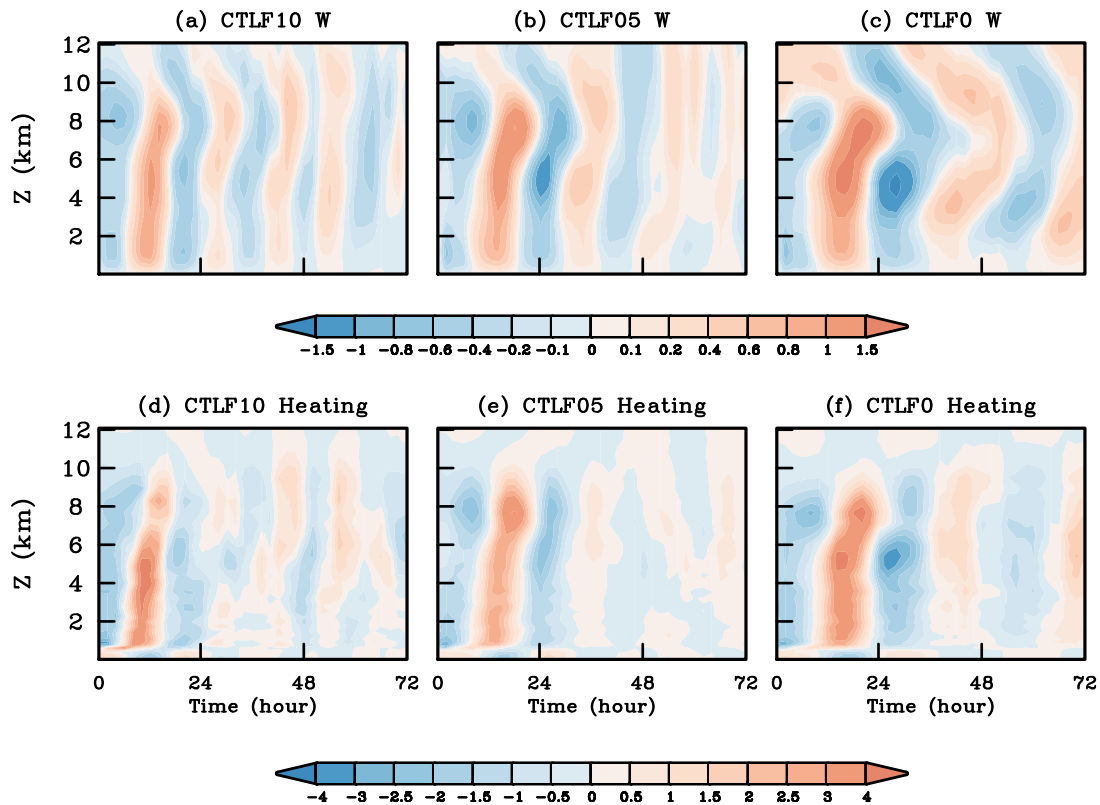
142

143 **Fig. 2** Plane views of water vapor path (kg m^{-2}) from 22 h to 52 h in CTLF10.

144

145 Meanwhile, we also present the time-height plots of vertical velocity and diabatic
146 heating averaged over the disturbed area during the whole simulation. Given that the
147 behavior of the disturbed columns exhibits a systematic tendency over the entire 3-day
148 duration of the simulations (Fig. S1), we use moving average method to filter out
149 variations longer than 30 hours. The filtered variables exhibit periodic features in the
150 central column of the domain (where the disturbance was initiated with the initial
151 moisture anomaly) across all simulations (Fig. 3). Based on the results after filtering,

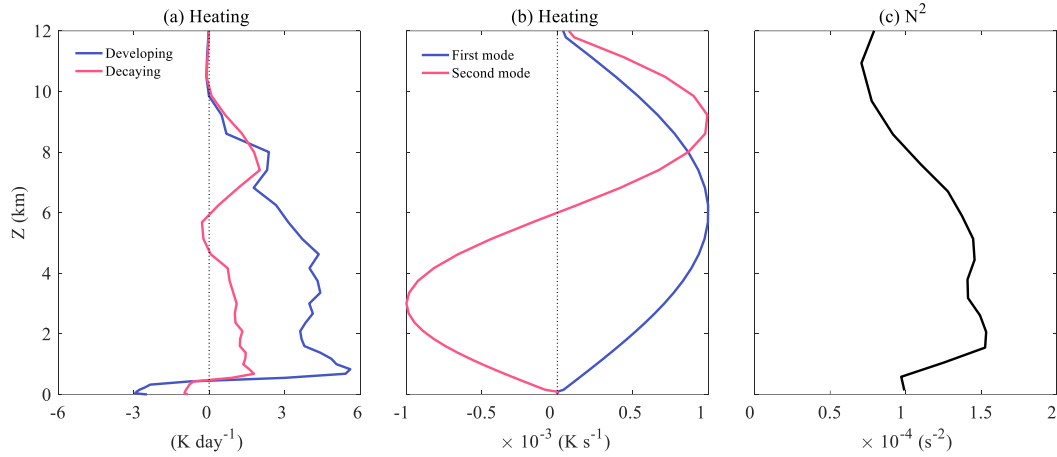
152 we define periods with positive heating and vertical velocity as the developing stages,
 153 while those with negative heating and vertical velocity are classified as the decaying
 154 stages. In CTLF10, the first developing stage occurs from 6 h to 16 h. The mean latent
 155 heating profile shows a vertical half-wavenumber structure in the free-troposphere
 156 (above the BL top). Unlike the first baroclinic mode observed in real-world scenarios
 157 (e.g., Haertel and Kiladis 2004; Houze, 2018), the latent heating here exhibits a bottom-
 158 heavy structure, with its maximum around 1 km altitude (Fig. 4a). The first decaying
 159 stage occurs from 16 h to 24 h, during which latent heating is significantly weaker
 160 compared to the developing stage. In this stage, the heating displays a more complicated
 161 vertical structure, characterized by heating from the BL top to 4.4 km, cooling from 4.4
 162 km to 5.8 km, and additional heating from 5.8 to 10 km height (Fig. 4a). Although the
 163 peak heating occurs in the upper troposphere, the vertical structure in this decaying
 164 stage does not clearly resemble the stratiform (wavenumber-one) structure seen in
 165 previous studies (e.g., Haertel and Kiladis 2004; Houze, 2018).
 166



167

168 **Fig. 3** Time-height plot of (a) vertical velocity (cm s^{-1}) and (d) diabatic heating

169 (K day⁻¹) in CTLF10, with signals longer than 30 hours filtered out. All the variables
 170 are averaged in the inner 150 km radii of the domain. (b), (e) and (c), (f) are for CTLF05
 171 and CTLF0, respectively.
 172



173

174 **Fig. 4** Vertical profiles of (a) the latent heating profiles averaged in the first developing
 175 (blue) and decaying (red) stage of CTLF10, (b) the first (blue) and second (red) diabatic
 176 heating mode (K s⁻¹) used in the dry simulations, and (c) the N² (s⁻²) in the initial field.
 177

178 In this first decaying stage, subsidence occurs in the lower levels of the disturbed
 179 column, extending from 6 km down to the surface (Fig. S1). This downward motion
 180 and the associated drying (between hours 16-24; Figs. 1b & 3) might be expected to
 181 inhibit subsequent convection at the same location (e.g., Houze, 1982; Houze, 2018).
 182 However, deep convection is reinvigorated after 24 hours, and the initially disturbed
 183 column repeats this cycle of developing and decaying convection over the next several
 184 days (Figs. 1 & 3). A similar pattern is seen in CTLF05 and CTLF0, although the
 185 periods of the cycles differ (Figs. 1 & 3).

186 The occurrence of periodic convection raises two questions: What mechanisms
 187 facilitate the recovery of deep convection following the downward motion in the
 188 disturbed air column? Additionally, what determines the period of the cycle? We will
 189 address these questions in the next two sections.

190

191 4. Convective recovery: the role of low-level buoyancy

192 To understand the recovery of convection after the decaying stage in the disturbed
 193 column, we need to understand the evolution of the variables that determine convective
 194 activity. Previous studies have demonstrated that low-level buoyancy plays a crucial
 195 role in determining precipitation in tropical MCDs (e.g., Ahmed and Neelin 2018;
 196 Ahmed et al. 2020). Following Ahmed et al. (2020), the low-level buoyancy of an
 197 entraining convective plume can be approximated as:

$$198 \quad B_{low} = g \left(w_1 \frac{\theta_{eBL} - \theta_{eL}^*}{\theta_{eL}^*} - w_2 \frac{\theta_{eL}^* - \theta_{eL}}{\theta_{eL}^*} \right), \quad (1)$$

199 in which θ_{eBL} is the BL averaged θ_e , θ_{eL} is the θ_e averaged in the lower free-
 200 troposphere, and θ_{eL}^* is the saturation θ_e in the lower free-troposphere. The first term
 201 on the right-hand side of Eq. (1) can be interpreted as an approximate measure of the
 202 undilute plume buoyancy based on BL properties and lower free-tropospheric
 203 temperature, and the second term measures the influence of lower free-tropospheric
 204 subsaturation on the plume via entrainment. The coefficients w_1 and w_2 are the weights
 205 of the two processes, which can be expressed as:

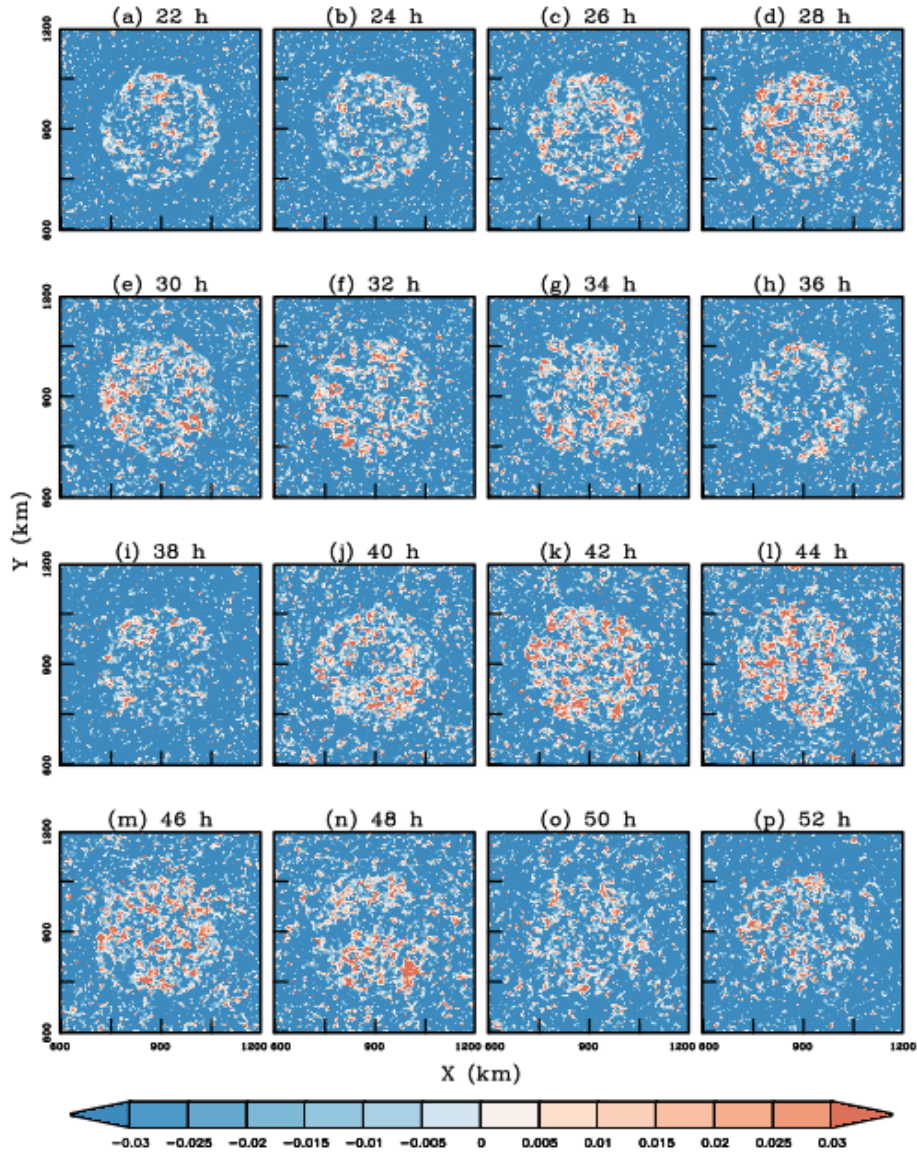
$$206 \quad w_1 = \frac{\Delta p_{BL}}{\Delta p_L} \ln \left(\frac{\Delta p_{BL} + \Delta p_L}{\Delta p_{BL}} \right),$$

$$207 \quad w_2 = 1 - w_1.$$

208 In this study, the BL and the low-level troposphere are defined as the layer below 900
 209 hPa and the layer between 900 hPa and 500 hPa, respectively. With this definition, w_1
 210 and w_2 are 0.4 and 0.6, respectively, but we follow parts of Ahmed et al. (2020) and
 211 henceforth use $w_1 = w_2 = 0.5$ to estimate the low-level buoyancy. All vertically averaged
 212 variables in Eq. (1) are density weighted.

213 The time evolution of B_{low} in the ‘CTL’ simulations is shown in Fig. 1c. In all
 214 three simulations, the evolution of B_{low} is in phase and strongly correlated with
 215 precipitation in the disturbance region after 12 hours. For comparison, plane views of
 216 B_{low} from 22 to 54 h in CTLF10 are also presented in Fig. 5. It is evident that the most

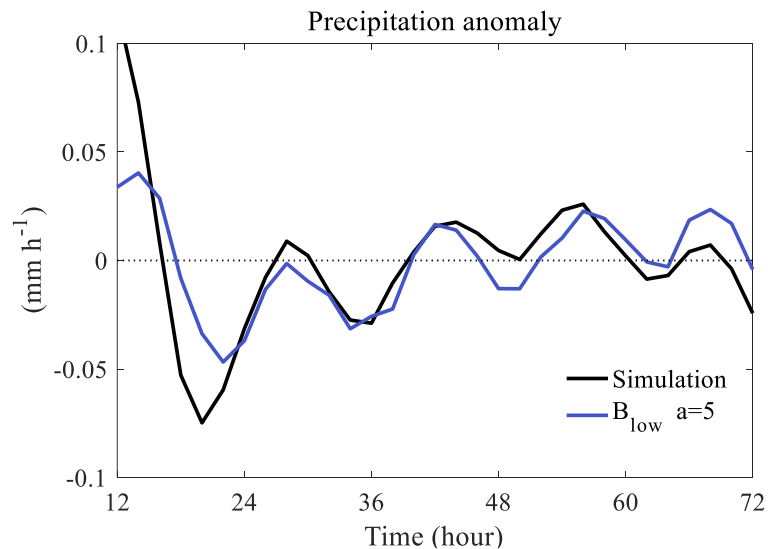
217 significant variations in B_{low} occur in the central column that was initially disturbed,
 218 which retains its size, shape, and location throughout the simulation. B_{low} shows an
 219 increasing trend from 22-28 h and 38-44 h, and a decreasing trend from 30-36h and 46-
 220 52h, consistent with the variations of precipitation and B_{low} shown in Fig. 1c.
 221



222
 223 **Fig. 5** Plane views of B_{low} (m s^{-2}) from 22 h to 52 h in CTLF10. We add a constant value
 224 of 0.05 to make B_{low} in the disturbance region around 0.

225
 226 To further investigate whether the evolution of B_{low} quantitatively reflects

227 precipitation changes, we reference the P- B_{low} relationship established in Ahmed et al.
 228 (2020, their Fig. 2) and find that sensitivity of $a=5$ (mm h^{-1}) (m s^{-2})⁻¹ provides an
 229 approximate fit in our simulations¹. Here, we calculate the precipitation anomaly using
 230 the variation of B_{low} in CTLF10, and compare it with the temporal precipitation
 231 anomaly from 0-72 h in CTLF10. As shown in Fig. 6, the temporal precipitation
 232 anomalies estimated from buoyancy variations are a close match to the explicitly
 233 simulated precipitation. This further validates the use of low-level buoyancy as a means
 234 of quantitatively understanding the evolution of convection in the disturbed column.
 235 Nonetheless, it is important to recognize that while B_{low} correlates well with
 236 precipitation, the absolute values do not always align. For instance, at 44 hours, B_{low}
 237 in CTLF0 is lower than in CTLF10, yet the precipitation in CTLF0 is greater (Fig. 1).
 238



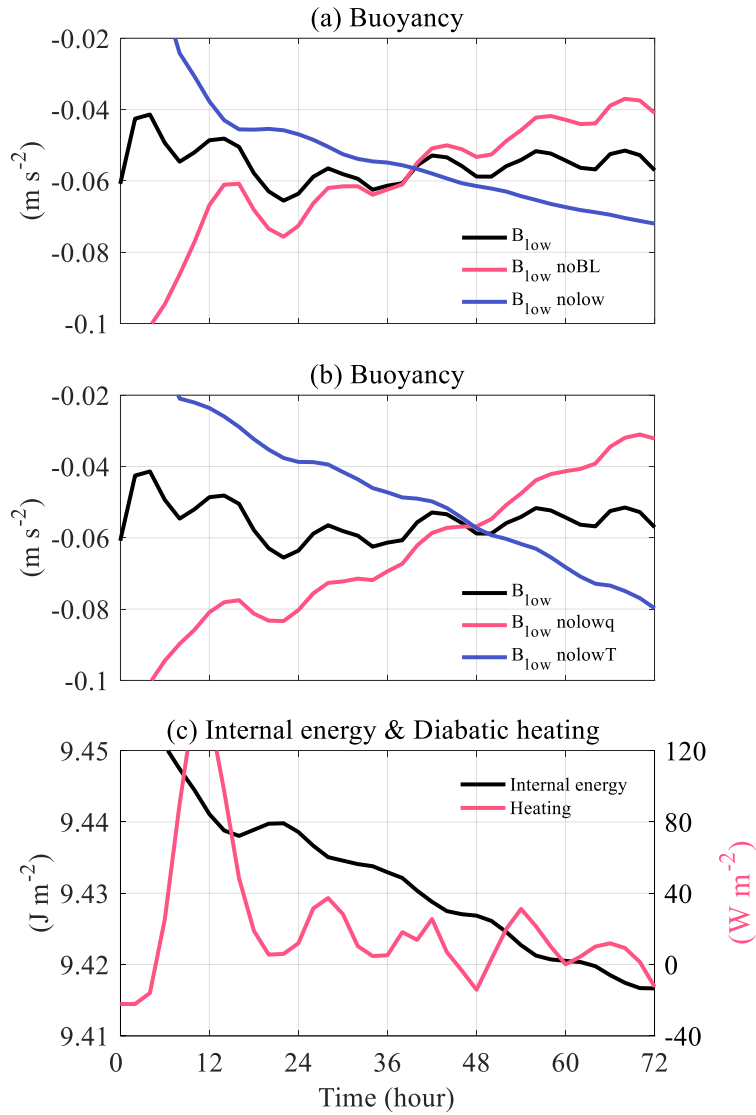
239
 240 **Fig. 6** Time series of temporal precipitation anomaly (mm h^{-1}) from 12-72 h in the
 241 disturbance in CTLF10 (black) and the precipitation anomaly estimated with low-level
 242 buoyancy (blue).

¹ Ahmed and Neelin (2020) found larger sensitivities of precipitation to buoyancy ($a=20$ (mm h^{-1}) (m s^{-2})⁻¹) than what we use here, but those were for positive buoyancies. In our simulations the precipitation occurs at weakly negative buoyancies, which is consistent with the smaller sensitivity we use here.

243

244 The above analysis indicates that, following the decay of the initial pulse of
245 precipitating convection, the recovery of low-level buoyancy is critical to the recovery
246 of deep convection and precipitation. According to equation (1), there are three factors
247 controlling the low-level buoyancy: the BL θ_e , the temperature in the lower free-
248 troposphere, and water vapor mixing ratio (q_v) in the lower free-troposphere. A higher
249 BL θ_e , a larger lower free-tropospheric humidity, or a colder lower free-tropospheric
250 temperature produce increased B_{low} . To identify which factor dominates the evolution
251 of B_{low} , we calculate B_{low} in CTLF10 again but substitute the BL θ_e with its
252 temporal mean from 0-72 h. Fixing the BL θ_e in Eq. (1) introduces a systematic trend
253 in B_{low} for the duration of the simulation, but retains the oscillation in B_{low} (Fig. 5a).
254 However, when the temperature and moisture variation in the lower free-troposphere is
255 removed using the same method, the oscillation in B_{low} greatly diminishes (Fig. 7a).
256 This indicates that for B_{low} to recover, it is the lower free-troposphere that matters most.

257



258

259 **Fig.7** (a) Time series of the original B_{low} (m s^{-2}) in CTLF10 (black), B_{low} calculated
 260 with a 0-72 h temporal mean BL variables (red), and B_{low} calculated with a 0-72 h
 261 temporal mean lower free-tropospheric variables (blue). (b) Time series of the original
 262 B_{low} in CTLF10 (black), B_{low} calculated with a 0-72 h temporal mean lower free-
 263 troposphere q_v (red), and B_{low} calculated with a 0-72 h temporal mean lower free-
 264 troposphere temperature (blue). (c) Time series of lower free-tropospheric mass-
 265 weighted internal energy (black, J m^{-2}) and diabatic heating (red, W m^{-2}).

266

267 We further investigate which characteristics in the lower free-troposphere

268 atmosphere is most significant in influencing the oscillation of B_{low} . We recalculated
269 B_{low} in CTLF10 by substituting the temperature and water vapor with their temporal
270 means from 0 to 72 hours. The results indicate that the oscillation of B_{low} is controlled
271 mostly by the temperature in the lower free-troposphere (Fig. 7b; the variance of the
272 detrended B_{low_nolowT} line in Fig. 7b is about one-third the variance of the detrended
273 B_{low_nolowq} line). This suggests that cooling in the lower free-troposphere is the
274 primary factor influencing B_{low} and, in turn, precipitation.

275 In this section, we demonstrated that the oscillation of deep convection and
276 precipitation can be explained by the oscillation of low-level buoyancy, which is
277 primarily influenced by variations in the lower free-troposphere temperature. However,
278 the mechanisms causing these temperature variations remain unclear. Previous
279 theoretical studies have argued that diabatic cooling in the lower free-troposphere by
280 stratiform convection can produce a decrease of lower free-tropospheric temperature
281 following deep convective heating (e.g., Mapes 2000; Kuang 2008b). However, in our
282 simulations, the diabatic cooling caused by stratiform precipitation is relatively weak.
283 In some cases, there is no discernible diabatic cooling in the lower free-troposphere
284 (e.g., CTLF05, Fig. S1e). Furthermore, Fig. 7c generally shows an out-of-phase
285 relationship (in a signal that is admittedly noisy) between temperature anomalies and
286 diabatic heating anomalies, with multiple instances of positive temperature tendency
287 anomalies occurring while diabatic heating anomalies are negative. This suggests that
288 the decrease of lower free-tropospheric temperature during the oscillation is not directly
289 caused by diabatic cooling of a stratiform heating structure. In the following section,
290 we will explore the occurrence of cooling in the lower free-troposphere and the
291 recovery of buoyancy from the perspective of adiabatic processes.

292

293 **5. Recovery of Buoyancy: an inertia-gravity oscillation**

294 In this section, we conduct a series of simulations without latent heating (or cooling),
295 termed ‘Dry’, to investigate the recovery of buoyancy in tropical MCDs after the

296 decaying stage (Table 1). These simulations have a domain size of 3000 km × 3000 km
 297 with open lateral boundary conditions. Additionally, there is no radiation or
 298 microphysics parameterization. The other settings remain consistent with the ‘CTL’
 299 series.

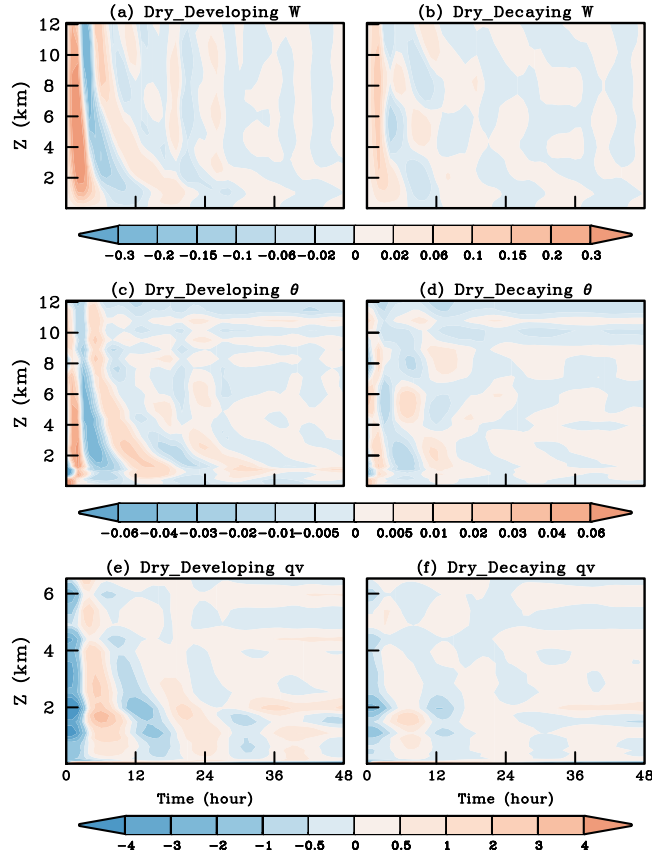
300 We first test the response of the disturbed column to heating in the developing
 301 (Dry_Developing) and decaying (Dry_Decaying) stage, as defined in section 3 (Fig.
 302 4a). In all the dry simulations, the imposed diabatic heating is maintained for two hours,
 303 followed by an additional 46 hours of simulation. In both Dry_Developing and
 304 Dry_Decaying, the diabatic heating produces subsequent damped oscillations of
 305 multiple variables including B_{low} (Figs. 8 and 9a). In real-world observations, tropical
 306 MCDs usually exhibit a half-wavenumber vertical structure during the development of
 307 deep convection, and a wavenumber-one vertical structure during the decay of deep
 308 convection (e.g., Haertel and Kiladis 2004; Houze 2018). To better understand the
 309 mechanism of the oscillation and to draw closer connections to real-world scenarios,
 310 we conduct a second set of dry simulations forced by a vertical wavenumber-one
 311 heating structure (‘Dry2’; Table 1).

312 The heating structure in the ‘Dry2’ simulations is given as follows:

$$Q(r, z) = \begin{cases} Q_0 \sin(2\pi z/H - \pi) \cos(\pi r/2R) & (z < H \text{ and } r < R) \\ 0 & (z \geq H \text{ or } r \geq R) \end{cases} \quad (2)$$

313 In Eq. (2), r and z represent radius and height, respectively. H and R are the maximum
 314 height and radius of the heating, which are 12 km and 150 km, respectively. Q_0 is the
 315 magnitude of the heating, which is set to be 0.001 K s⁻¹. This heating has a typical
 316 second baroclinic mode (stratiform heating profile) in the vertical direction (Fig. 4b),
 317 which also decays sinusoidally with radius. The magnitude of the heating is chosen to
 318 be roughly 20 times stronger than the diabatic heating in the developing phase of the
 319 full-physics model (Fig. 4a) to both better match diabatic heating values in observed
 320 real-world synoptic systems and obtain a better signal-to-noise ratio (simulations using
 321 a weaker forcing with magnitude of 1 × 10⁻⁴ K s⁻¹ produces qualitatively similar results).

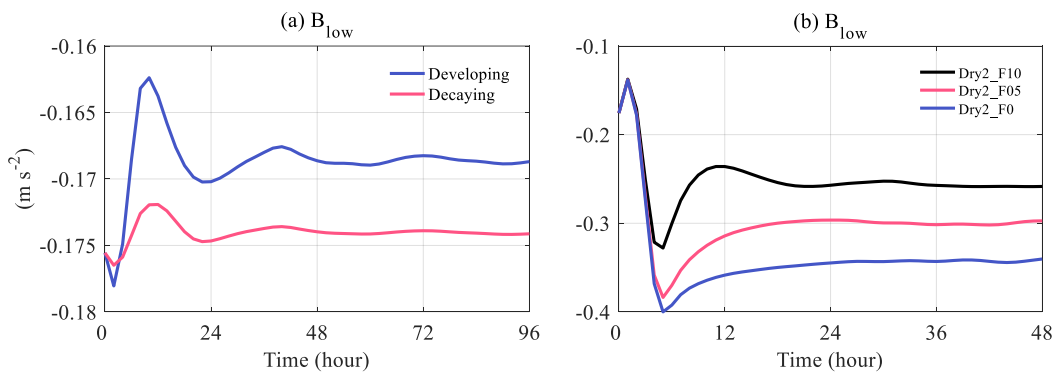
322



323

324 **Fig. 8** The time-height plot of (a) vertical velocity (cm s^{-1}), (c) temporal potential
 325 temperature anomaly (K), and (e) temporal q_v anomaly (g kg^{-1}), all averaged in the inner
 326 150 km radii of the central column in Dry_Developing. (b), (d) and (f) are for
 327 Dry_Decaying.

328

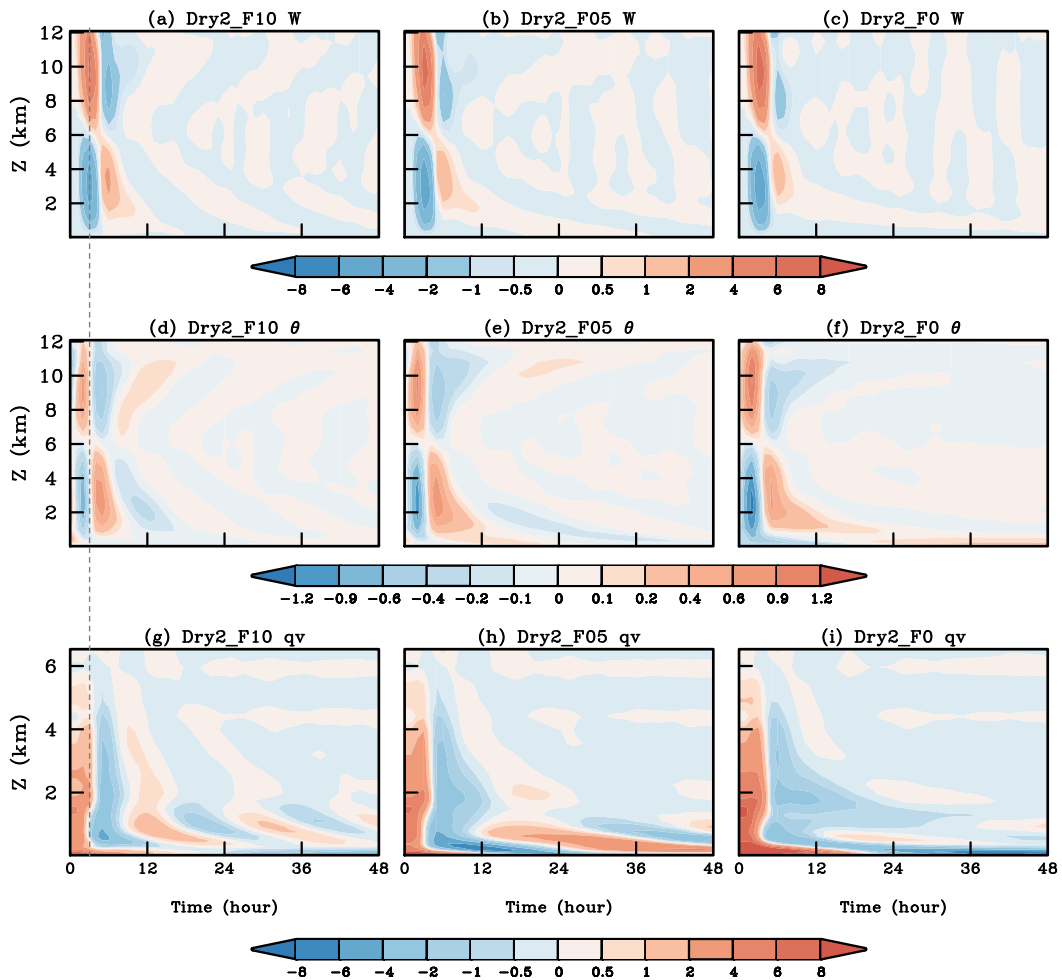


329

330 **Fig. 9** (a) Time series of B_{low} (m s^{-2}) in Dry_Developing (blue) and Dry_Decaying
 331 (red). (b) Time series of B_{low} (m s^{-2}) in Dry2_F10 (black), Dry2_F05 (red), and
 332 Dry2_F0 (blue).

333

334 The immediate response of the air column in Dry2_F10 to the heating is
 335 characterized by upward motion above 6 km and downward motion below 6 km (Fig.
 336 10a). Although these vertical motions may induce adiabatic cooling at upper levels and
 337 warming at lower levels, they are insufficient to offset the diabatic heating and cooling
 338 over such a short time frame. Consequently, warm and cold anomalies develop at 9 km
 339 and 3 km, respectively, during the initial hours (Fig. 10d). Additionally, the vertical
 340 motion redistributes water vapor, with subsidence over the first several hours inducing
 341 a drying tendency at lower levels (in Fig. 10 we subtracted the time-mean values to
 342 obtain anomalies, so a secular drying trend over the course of the simulation yields an
 343 moist anomaly during the initial few hours that decays in response to the subsidence).
 344



345
 346 **Fig. 10** The time-height plot of (a) vertical velocity (cm s^{-1}), (d) temporal potential
 347 temperature anomaly (K), and (g) temporal q_v anomaly (g kg^{-1}), all averaged in the inner

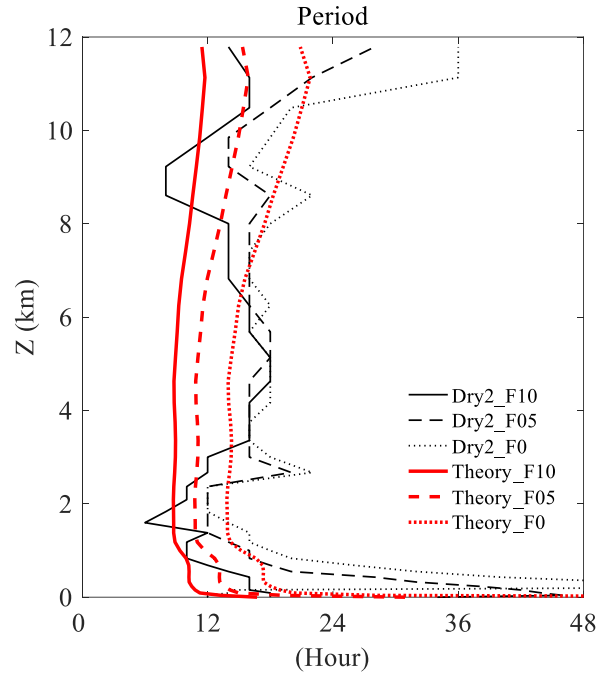
348 150 km radii of the domain in Dry2_F10. (b), (e), (h) and (c), (f), (i) are for Dry2_F05
349 and Dry2_F0, respectively. The vertical dashed line marks the moment that the vertical
350 velocity in the lower free-troposphere reaches the first minimum, indicating that the
351 temperature and q_v anomaly is 1/4 period behind the vertical velocity.

352

353 Although the diabatic heating ceases after 2 hours, the response of vertical motion
354 persists for a significantly longer duration. The evolution of temperature and q_v lags the
355 vertical velocity by one-fourth of the oscillation period, suggesting that vertical motion
356 is the driving force behind the changes in temperature and q_v . The subsidence in the
357 lower free-troposphere further results in warming and drying at lower levels, which
358 decreases low-level buoyancy that would be expected to suppress convection in a
359 simulation with latent heating (Fig. 9b). However, the vertical motion reverses 6 hours
360 after model initialization (4 hours after the cessation of the diabatic forcing), resulting
361 in a cooler and moister lower troposphere that enhances B_{low} (Fig. 9b). In fact, the
362 vertical motion undergoes periodic sign changes, leading to oscillations in temperature
363 and q_v (Figs. 10a, d, & g), and, in turn, B_{low} (Fig. 9b). In Dry2_F05 and Dry2_F0, we
364 also find similar oscillations (Figs. 9b & 10). The oscillation period increases as the
365 Coriolis parameter decreases, consistent with the results of the full-physics simulations
366 (Fig. 1). It is important to note that in all the dry simulations, the oscillation period
367 varies with altitude (Fig. 10). The profile of the period generally exhibits a ‘C’ shape
368 (Fig. 11), characterized by shorter periods throughout most of the troposphere and
369 longer periods in the upper troposphere and the lowest kilometer (here the period is
370 defined as the time between the first two same-signed vertical velocity extrema). This
371 vertical structure of the period also corresponds to an increase in vertical wavenumber
372 over time (Fig. 10).

373

374



375

376 **Fig. 11** Vertical profiles of period (hour) in Dry2_F10 (black solid), Dry2_F05 (black
 377 dashed) and Dry2_F0 (black dotted). Red lines are their counterparts estimated by the
 378 linear theory.

379

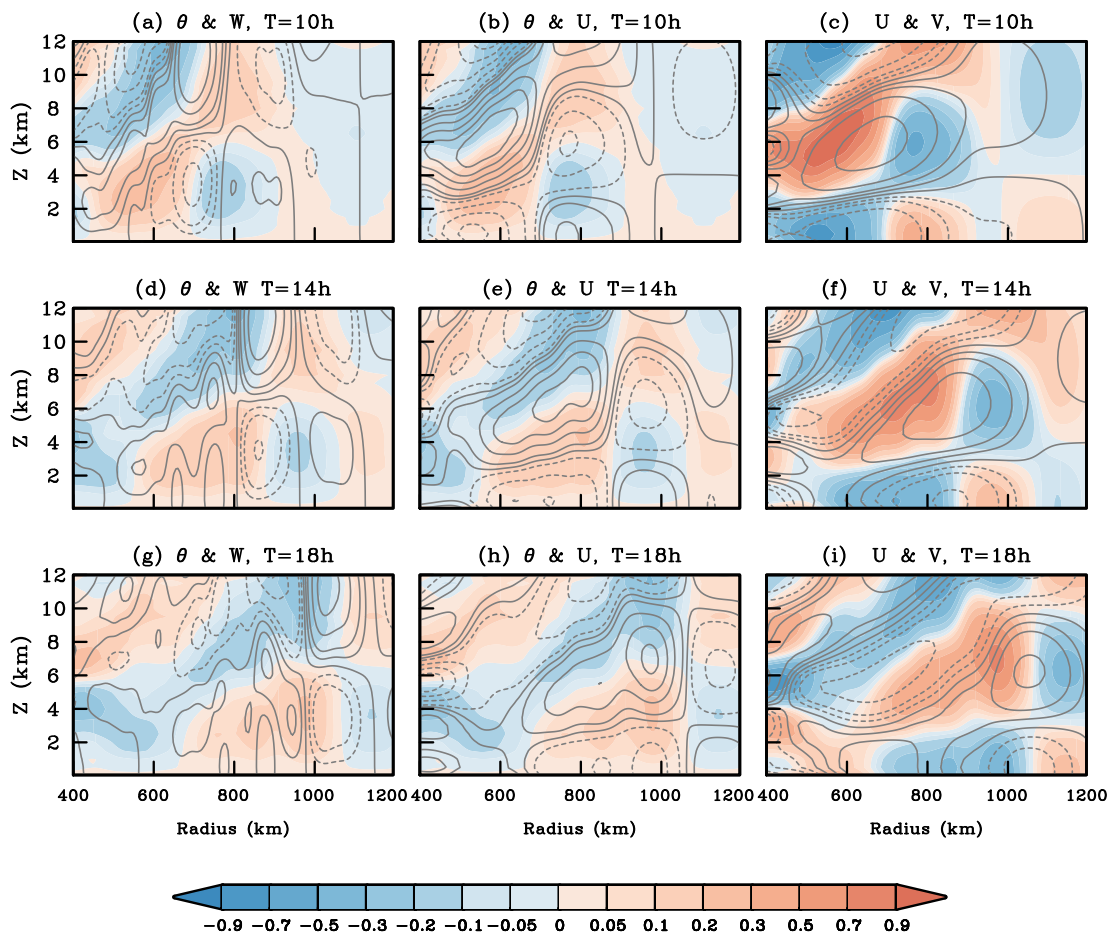
380 We have shown that in dry simulations, an air column perturbed by a stratiform
 381 heating profile exhibits internal damped oscillations, which alter low-level buoyancy in
 382 ways that would be expected to support oscillations of precipitating convection if
 383 condensation occurred. Given that the simulations are conducted on an f-plane within
 384 a stratified atmosphere, these oscillations are likely inertia-gravity oscillations. It is
 385 well-known that an air column undergoing oscillations usually triggers waves, which
 386 are characterized by specific spatial structures of dynamical and thermodynamic
 387 variables. To confirm the inertia-gravity nature of the oscillation, we will now study
 388 the property of the waves triggered by the oscillation and compare the characteristics
 389 with linear inertia-gravity wave theory.

390 The radius-height structures of several key variables outside the disturbance region
 391 in Dry2_F10, as shown in Fig. 12, indicate an outward propagating wave signal. The
 392 first wave front at 10 h exhibits subsidence at upper levels and ascent at lower levels at
 393 radii between 400-500 km, and consists of an outward-propagating structure with

394 respective warm and cold anomalies one-fourth of a wavelength behind the vertical
 395 motion (Figs. 10a, d & g). This structure aligns with findings from previous studies
 396 (e.g., Nicholls et al. 1991; Mapes 1993).

397 In a linear inertia-gravity wave, when a cold anomaly is situated above a warm
 398 anomaly, ascent and outward radial velocity anomalies should exist between these
 399 temperature anomalies (e.g., Fig. 5.12 of Holton and Hakim 2012). The left and middle
 400 columns in Fig. 12 illustrate that the relationships between temperature and vertical and
 401 radial velocity are consistent with this theoretical expectation. Furthermore, theory
 402 predicts that tangential velocity maxima should occur where the radial velocity changes
 403 sign. As depicted in the right column of Fig. 12, a similar phase relationship is seen in
 404 the Dry2_F10 simulation. The similarity of the wave structure with linear theory
 405 reinforces the conclusion that the oscillations produced by the initial diabatic forcing in
 406 the dry simulations are inertia-gravity oscillations

407

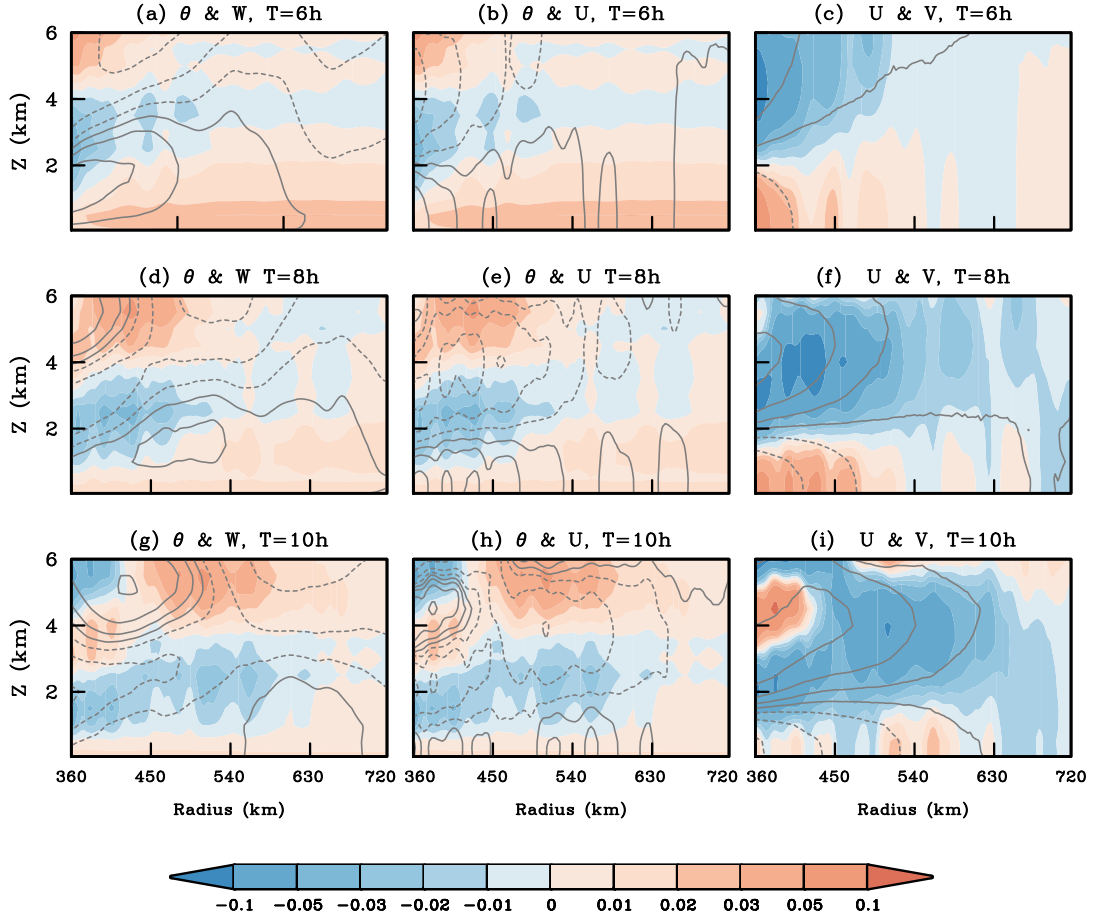


408

409 **Fig. 12** Radius-height plots of azimuthal-mean of (a) horizontal potential temperature
410 anomaly (K, shading) and vertical velocity (contour at -3, -2, -1, -0.5, 0, 0.5, 1, 2 and 3
411 cm s^{-1}), (b) horizontal potential temperature anomaly (K, shading) and radial velocity
412 (contour at 0.9, -0.7, -0.5, -0.3, -0.1, 0, 0.1, 0.3, 0.5, 0.7 and 0.9 m s^{-1}), and (c) radial
413 velocity (cm s^{-1} , shading) and tangential velocity (contour at -0.6, -0.4, -0.2, -0.1, -0.05,
414 0, 0.05, 0.1, 0.2, 0.4 and 0.6 m s^{-1}). The upper, middle and lower panel are for 10 h, 14
415 h and 18 h in Dry2_F10, respectively.

416

417 For comparison, we present radius-height plots of the same variables from the full-
418 physics simulation CTLF10 (Fig. 13). Due to a systematic warming tendency above 7
419 km, which may obscure the wave signal, we focus only on the structures below 6 km.
420 In CTLF10, diabatic heating does not have the simple, idealized vertical structure
421 imposed in the dry simulations, so the wave structures are not as clearly defined as
422 those in the dry simulations. Nevertheless, several dominant features of inertia-gravity
423 waves remain evident. For instance, downward motion consistently precedes the warm
424 anomaly, the phase lines separating cold and warm anomalies align with peak radial
425 velocity anomalies, and the tangential velocity maxima correspond to points where the
426 radial velocity changes sign. These features suggest that even in full-physics
427 simulations, the oscillation generally retains its inertia-gravity characteristics.



428
429 **Fig. 13** As in Fig.12, but for CTLF10 at 6 h (upper) 8 h (middle) and 10 h (lower).

430
431 While the structure of the wave aligns with inertia-gravity wave theory, more
432 quantitative evidence would come from consistency in the dispersion relationship.
433 According to linear inertia-gravity wave theory,

$$434 \quad \nu^2 = f^2 + N^2(k^2 + l^2)m^{-2} \quad (3)$$

435 In Eq. (3), ν is the frequency of the oscillation, f is the Coriolis parameter and N^2 is the
436 buoyancy frequency. k and l are wavenumbers in the x and y directions, respectively,
437 and $k^2 + l^2$ is thus the square of the wavenumber in the radial direction. m is the
438 wavenumber in the vertical direction.

439 Since we have applied a stratiform heating structure in the disturbance as shown in
440 Fig. 4b, the wavelength in the vertical direction should be 12 km. Potential temperature,
441 vertical motion, and radial velocity exhibit a radial wavelength of around 600 km (Fig.
442 12), consistent with a linear response to the forcing which has that same wavelength

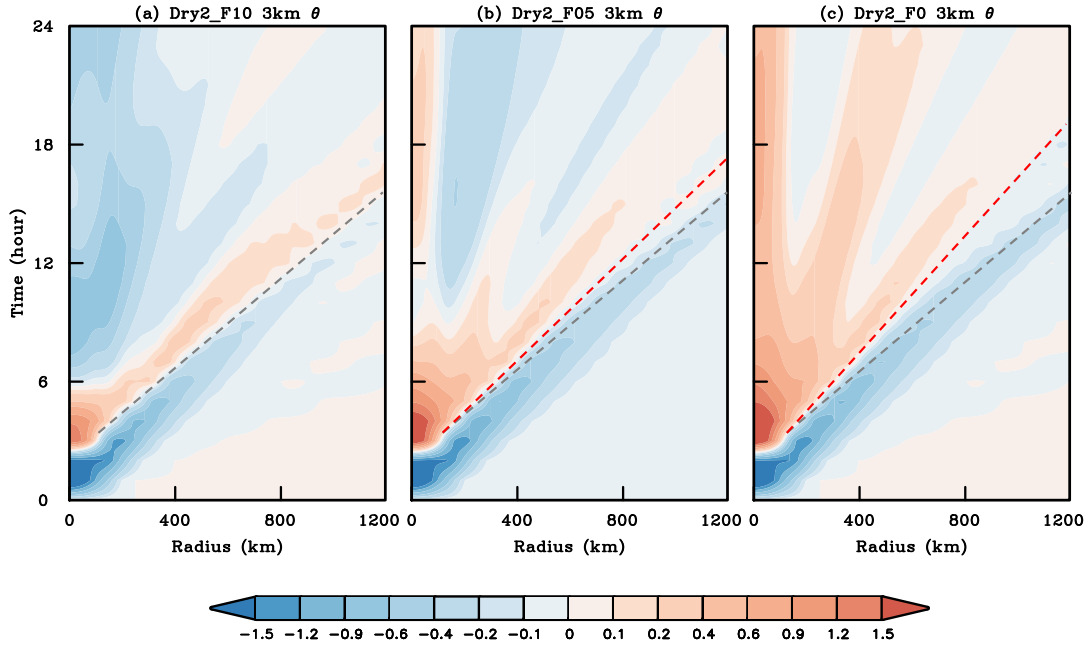
443 (the diameter of the impose heating is 300 km, so the wavelength trigger by the heating
 444 should be 600 km). However, the tangential velocity displays a slightly longer
 445 wavelength (Figs. 12f & h), so we use a general wavelength of 750 km with the profile
 446 of N^2 (Fig. 4c) to estimate the oscillation period using Eq. (3). The estimated
 447 oscillation period is similar to the period simulated in Dry2_F10 (Fig. 11) and exhibits
 448 slightly larger values in the upper troposphere and substantially larger values just above
 449 the surface, due to smaller values of N^2 at both upper and lower altitudes. Since the
 450 horizontal wavelengths in Dry2_F05 and Dry2_F0 are slightly longer compared to
 451 those in Dry2_F10 (Figs. 14), we estimate the general wavelengths in Dry2_F05 and
 452 Dry2_F10 to be 900 km and 1050 km, respectively, and the estimated periods are also
 453 consistent with those observed in the dry simulations (Fig. 11).

454 From the dispersion relationship, we can further infer the phase speed of the wave.
 455 The phase speed is written as:

$$456 \quad c = v / \sqrt{k^2 + l^2} \quad (4)$$

457 We substituted the respective periods and wavelength of Dry2_F10, Dry2_F05,
 458 and Dry2_F0 at a height of 3 km (10, 15, and 18 hours, respectively, as shown in Fig.
 459 11) into Eq. (4). This yielded theoretical phase speeds of 20.8 m/s, 16.7 m/s, and 16.2
 460 m/s, respectively. As illustrated in Figs. 14a-c, the phase speeds of the first wave front
 461 in Dry2_F10, Dry2_F05, and Dry2_F0 are 22.4 m/s, 20.8 m/s, and 18.2 m/s,
 462 respectively (these phase speeds were obtained by fitting a line to the zero θ anomaly
 463 shown in Fig. 14). Overall, the theoretical phase speeds are close to those observed in
 464 the dry simulations, further confirming that the column being disturbed is doing inertia-
 465 gravity oscillation.

466



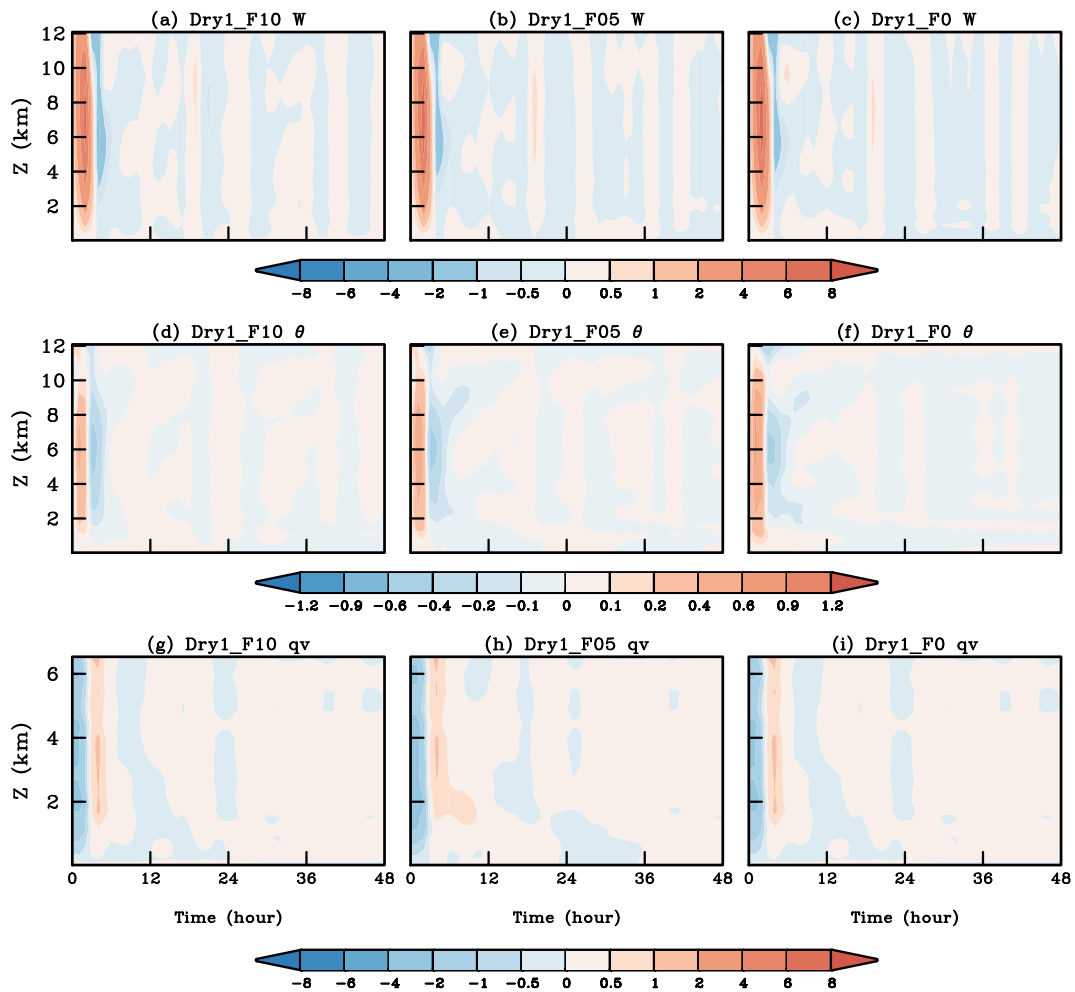
467

468 **Fig. 14** Radius–time Hovmöller diagram of the azimuthal-mean of horizontal potential
 469 temperature anomaly (K) at 3 km height in (a) Dry2_F10, (b) Dry2_F05 and (c)
 470 Dry2_F0. The dashed black lines show the phase line where potential temperature
 471 anomaly changes sign in Dry2_F10, and the dashed red lines show those in Dry2_F05
 472 and Dry2_F0, respectively.

473

474 Finally, we examine the response of the dry atmosphere to the first baroclinic
 475 heating mode, as this heating mode is also a dominant feature in tropical MCDs. The
 476 set of ‘Dry1’ simulations is designed similarly to the ‘Dry2’ simulations (Table 1), with
 477 the only difference being the application of the first baroclinic heating mode in the
 478 vertical direction (Fig. 4b). Upon model initialization, the deep heating triggers upward
 479 motion throughout the entire column (Figs. 15a-c). Although this upward motion
 480 induces adiabatic cooling, it is insufficient to counterbalance the diabatic heating,
 481 resulting in warming across the entire column during the first 2 hours (Figs. 15d-f).
 482 After the heating ceases, the upward motion continues, cooling and moistening the
 483 lower atmosphere. This free-tropospheric cooling and moistening would be expected to
 484 invigorate deep convection and prolong the presence of the first heating mode in full-
 485 physics simulations. After 6 hours, the vertical velocity becomes negative in the
 486 disturbance region (Figs. 15a-c), which reduces the cold and wet anomalies in the

487 column (Figs. 15d-i). However, there is no clear recovery of upward motion or low-
 488 level buoyancy following this subsidence, so that any oscillation is sufficiently damped
 489 so as to exist for only one period. Furthermore, the magnitude of the response in the
 490 ‘Dry1’ simulations is significantly smaller than that of the ‘Dry2’ simulations. These
 491 results strongly suggest that it is the second baroclinic heating mode that is responsible
 492 for the inertia-gravity oscillation, especially in real-world scenarios.
 493



494 **Fig. 15** As in Fig. 6, but for Dry1_F10, Dry1_F05 and Dry1_F0.
 495
 496

497 From the dry simulations in this section, we have demonstrated that in a
 498 background with rotation and stratification, an air column disturbed by mesoscale
 499 diabatic heatings can lead to oscillations, with the underlying mechanism being an
 500 inertial-gravity oscillation. In real-world scenarios, the stratiform heating profile plays

501 a crucial role in the recovery of low-level buoyancy. Although the immediate response
502 to the stratiform cooling in the lower free-troposphere does not favor low-level
503 buoyancy recovery, the inertia-gravity oscillation triggered by stratiform heating soon
504 results in ascent at the lower levels of the disturbed air column. This upward motion
505 cools and moistens the lower atmosphere, facilitating the recovery of low-level
506 buoyancy and, consequently, initiating a new episode of deep convection.

507 During such oscillation of convective disturbances, diabatic heating serves not only
508 as a source for the subsequent oscillations of the air column but also as a consequence
509 of the preceding oscillations. The wave source—namely, the convective heating—
510 redevelops with each oscillation period, thereby establishing this phenomenon as a
511 convectively coupled inertia-gravity oscillation. While an air column's oscillation
512 within a "convectively coupled inertia-gravity wave" might also be termed a
513 "convectively coupled inertia-gravity oscillation," the phenomenon identified in our
514 study is fundamentally different. In the context of a "convectively coupled inertia-
515 gravity wave," local convective oscillations are driven by external large-scale wave
516 propagation. However, the convective oscillation seen in our research is internally
517 generated. To distinguish this phenomenon from concepts presented in previous studies,
518 we refer the oscillation in this study as a "convectively coupled internal oscillation."

519

520 **6. Discussion and Summary**

521 Gravity waves serve as a crucial link between convective disturbances and their
522 surrounding environments. On one hand, large-scale waves propagating across a region
523 may produce quasi-periodic behavior of convection in that region by modifying the
524 environmental conditions (e.g., Haertel and Kiladis 2004; Kuang 2008a; Kuang 2010;
525 Tulich and Mapes 2010). On the other hand, latent heating within a convective
526 disturbance can also initiate gravity waves that propagate away from the disturbance.
527 While research on such convectively generated waves typically focuses on how these
528 waves affect the remote environment—such as by radiating momentum and energy
529 away from the disturbance (e.g., Bretherton and Smolarkiewicz 1989; Nicholls et al.
530 1991; Mapes 1993)—the influence of these waves on the subsequent behavior of the

531 convective disturbance has received comparatively little attention. A useful analogy is
532 that of a stone dropped into a calm pond: the disturbed water column not only generates
533 gravity waves that propagate outward, but itself continues to oscillate after the initial
534 disturbance.

535 In this study, we employ a series of idealized convective-permitting simulations to
536 investigate the evolution of an atmospheric column being disturbed. Full-physics
537 simulations demonstrate that the disturbed column typically exhibits internal damped
538 oscillations in convective activity. Detailed analysis reveals that the oscillations in
539 convection are primarily driven by oscillations in low-level buoyancy, which in turn
540 arise from oscillations in temperature and moisture in the lower free-troposphere. By
541 comparing dry simulations with linear gravity wave theory, we further show that the
542 oscillations in lower-tropospheric temperature and moisture within the disturbed
543 column are a consequence of inertia-gravity oscillations forced by an initial pulse of
544 diabatic heating.

545 The convective oscillation seen in our research is internally generated, during
546 which diabatic heating serves not only as a source for the subsequent inertia-gravity
547 oscillations of the air column but also as a consequence of the preceding oscillations.
548 Although inertia-gravity oscillations and convection can occur almost anywhere on
549 Earth, we suggest that "mesoscale" convective disturbances over "tropical" oceans offer
550 more favorable conditions for this oscillation to occur. Regarding disturbance size, a
551 disturbance that is too small corresponds to a high frequency, which may be easily
552 damped, while a disturbance too large tends to achieve a quasi-geostrophic balance,
553 rendering convergence negligible. Environmentally, tropical oceans supply substantial
554 surface water vapor flux, enhancing the efficiency of low-level upward motion in
555 increasing low-level buoyancy.

556 Two important points are highlighted from this research. The first is the critical role
557 of low-level buoyancy in the life cycle of convective disturbances. In previous studies,
558 latent heat release in convective disturbances is often linked to BL convergence. This
559 concept has been incorporated into many cumulus parameterizations (e.g., Hayashi and

560 Sumi 1986; Lau and Peng1987), but can lead to unphysical growth at the finest scales
561 (sometimes termed the CISK catastrophe, e.g., Crum and Dunkerton 1992; Matthews
562 and Lander 1999). Recent studies by Liu et al. (2019, 2022) proposed that latent heat
563 release actually lags BL convergence, and cumulus parameterizations accounting for
564 this time lag yield significantly better performance. Here we provide evidence that the
565 variation of precipitation in a tropical MCD is not directly controlled by changes in the
566 BL, but by variations in lower-free tropospheric buoyancy. In our simulations, the time
567 lag identified in Liu et al. (2019, 2022) would represent the time required for the system
568 to transition from a low-level vertical velocity maximum to a temperature minimum,
569 approximately one-fourth of the oscillation period (Fig. 7). Thus, recognizing the
570 critical role of low-level buoyancy provides insights for improving cumulus
571 parameterizations, especially for those based on the ‘wave-CISK’ perspective.

572 Our second important point concerns the critical role of stratiform heating in real-
573 world tropical MCDs. Although stratiform heating initially leads to lower-tropospheric
574 subsidence and a reduction in lower-tropospheric buoyancy, which does not favor
575 convection, the subsequent phase of the oscillation results in upward motion and a
576 recovery of buoyancy that triggers the next episode of convection. Compared to deep
577 convective heating, stratiform heating is more effective in inducing oscillations. This
578 sensitivity arises from the larger vertical wavenumber associated with stratiform
579 heating, which results in slower outward propagation of energy, allowing more energy
580 to remain available for maintaining the oscillation of the air column (e.g., Wu 2000;
581 2003). In real-world scenarios, stratiform heating is typically weaker than deep
582 convective heating, making the internal oscillation susceptible to contamination and
583 influence from other signals, such as large-scale waves and the diurnal cycle of
584 insolation. Therefore, tropical MCDs with stronger intensity are more likely to exhibit
585 an internal quasi-periodic oscillation. In separate work, we will examine the role of this
586 internal quasi-periodic oscillation in tropical cyclone precursors.

587 The internal oscillation identified here offers a new perspective for understanding
588 and predicting the variations of observed tropical MCDs. The interaction of tropical

589 MCDs with other periodic forcings might be interpreted as the superposition of the
590 internal and forced oscillations, with differing amplitudes and periods. For example,
591 the internal oscillation of an MCD that serves as a TC precursor could interact with the
592 diurnal cycle of insolation, accelerating or delaying TC genesis depending on the phase
593 of the superposition. To fully understand the internal oscillation, we need to identify the
594 factors influencing the oscillation period. This study indicates that, in addition to the
595 Coriolis parameter and stratification, a significant influence may arise from the
596 coupling of convection. When coupled with convection, the recovery of low-level
597 buoyancy occurs more swiftly than in dry cases, particularly when the Coriolis
598 parameter is smaller (Figs. 1c, 9b). This interplay of convection complicates the
599 oscillation, necessitating further investigation.

600

601 **Acknowledgement**

602 We would like to thank Prof. David Neelin, Prof. Zhaohua Wu, Prof. Zhuo Wang and
603 Dr. Hao Fu for useful discussions. This work is jointly supported by the National
604 Natural Science Foundation of China 42205004, the China Postdoctoral Science
605 Foundation 2024T170011 and the China Scholarship Grant 202406010151. We thank
606 for the technical support of the National Large Scientific and Technological
607 Infrastructure “ Earth System Numerical Simulation Facility ”
608 (<https://cstr.cn/31134.02.EL>).

609

610 **Data availability statement.**

611 All data and software for this paper are properly cited and referred to: the Jordan
612 sounding found in Jordan (1958) and the WRF model found in Skamarock et al. (2019).

613

614

615 **Reference**

- 616 1. Ahmed, F., and J. D. Neelin, 2018: Reverse engineering the tropical precipitation–
617 buoyancy relationship. *J. Atmos. Sci.*, **75**, 1587–1608.
- 618 2. Ahmed, F., Á. F. Adames, and J. D. Neelin, 2020: Deep Convective Adjustment of
619 Temperature and Moisture. *J. Atmos. Sci.*, **77**, 2163–2186.
- 620 3. Bretherton, C. S., and P. K. Smolarkiewicz, 1989: Gravity Waves, Compensating
621 Subsidence and Detrainment around Cumulus Clouds. *J. Atmos. Sci.*, **46**, 740–759.
- 622 4. Browner, S. P., W. L. Woodley, and C. G. Griffith, 1977: Diurnal oscillation of the
623 area of cloudiness associated with tropical storms. *Mon. Wea. Rev.*, **105**(7), 856–
624 864.
- 625 5. Crum, F. X., and T. J. Dunkerton, 1992: Analytic and numerical models of wave–
626 CISK with conditional heating. *J. Atmos. Sci.*, **49**, 1693–1708.
- 627 6. Diaz, M., and W. R. Boos, 2021a: Evolution of idealized vortices in monsoon-like
628 shears: Application to monsoon depressions. *J. Atmos. Sci.*, **78**, 1207–1225.
- 629 7. Diaz, M., and W. R. Boos, 2021b: The influence of surface heat fluxes on the
630 growth of idealized monsoon depressions. *J. Atmos. Sci.*, **78**, 2013–2027.
- 631 8. Dunion, J. P., C. D. Thorncroft, and C. S. Velden, 2014: The Tropical Cyclone
632 Diurnal Cycle of Mature Hurricanes. *Mon. Wea. Rev.*, **142**, 3900–3919.
- 633 9. Emanuel, K., 2018: 100 years of progress in tropical cyclone research. *Meteorol.*
634 *Monogr.*, **59**, 11–15.
- 635 10. Fingerhut, W. A., 1978: A Numerical Model of a Diurnally Varying Tropical Cloud
636 Cluster Disturbance. *Mon. Wea. Rev.*, **106**, 255–264.
- 637 11. Gray, W. M., and R. W. Jacobson Jr., 1977: Diurnal variation of deep cumulus
638 convection. *Mon. Wea. Rev.*, **105**, 1171–1188.
- 639 12. Haertel, P. T., and R. H. Johnson, 1998: Two-day disturbances in the equatorial
640 western Pacific. *Quart. J. Roy. Meteor. Soc.*, **124**, 615–636.
- 641 13. Haertel, P. T., and G.N. Kiladis, 2004: Dynamics of 2-day equatorial waves. *J.*
642 *Atmos. Sci.*, **61**, 2707–2721.
- 643 14. Hayashi, Y., and A. Sumi, 1986: The 30–40 day oscillations simulated in an “aqua-

- 644 planet” model. *J. Meteor. Soc. Japan*, **64**, 451–467.
- 645 15. Holton, B. J. R. and G. J. Hakim, 2012: An Introduction to Dynamic Meteorology.
646 5th ed. Academic Press, 535 pp.
- 647 16. Hong, S. Y., Y. Noh, and J. Dudhia, 2006: A new vertical diffusion package with an
648 explicit treatment of entrainment processes. *Mon. Wea. Rev.*, **134**, 2318–234.
- 649 17. Houze, R. A., 1982: Cloud clusters and large-scale vertical motions in the tropics.
650 *J. Meteor. Soc. Japan*, **60**, 396–410
- 651 18. Houze, R. A., 2018: 100 Years of Research on Mesoscale Convective
652 Systems. *Meteor. Monogr.*, **59**, 17.1–17.54.
- 653 19. Iacono, M. J., J. S. Delamere, E. J. Mlawer, M. W. Shephard, S. A. Clough, and W.
654 D. Collins, 2008: Radiative forcing by long-lived greenhouse gases: Calculations
655 with the AER radiative transfer models. *J. Geophys. Res.*, **113**, D13103.
- 656 20. Jordan, C. L., 1958: Mean soundings for the West Indies area. *J. Meteor.*, **15**, 91–
657 97.
- 658 21. Klemp, J. B., and D. K. Lilly, 1978: Numerical simulation of hydrostatic mountain
659 waves, *J. Atmos. Sci.*, **35**, 78–107.
- 660 22. Kuang, Z., 2008: A moisture-stratiform instability for convectively coupled waves.
661 *J. Atmos. Sci.*, **65**, 834–854.
- 662 23. Kuang, Z., 2010: Linear Response Functions of a Cumulus Ensemble to
663 Temperature and Moisture Perturbations and Implications for the Dynamics of
664 Convectively Coupled Waves. *J. Atmos. Sci.*, **67**, 941–962.
- 665 24. Lau, K., and L. Peng, 1987: Origin of Low-Frequency (Intraseasonal) Oscillations
666 in the Tropical Atmosphere. Part I: Basic Theory. *J. Atmos. Sci.*, **44**, 950–972
- 667 25. Li, T., X. Ge and B. Wang, 2006: Tropical cyclogenesis associated with Rossby
668 wave energy dispersion of a preexisting typhoon. Part II: Numerical simulations. *J.*
669 *Atmos. Sci.*, **63**, 1390–1409.
- 670 26. Liu, Y., Z. Tan, and Z. Wu, 2019: Noninstantaneous wave-CISK for the interaction
671 between convective heating and low-level moisture convergence in the tropics. *J.*
672 *Atmos. Sci.*, **76**, 2083–2101.

- 673 27. Liu, Y., Z. Tan, and Z. Wu, 2022: Convective Response in a Cloud-Permitting
674 Simulation of the MJO: Time Scales and Processes. *J. Atmos. Sci.*, **79**, 1473–1490.
- 675 28. Matthews, A. J., and J. Lander, 1999: Physical and numerical contributions to the
676 structure of Kelvin wave-CISK modes in a spectral transform model. *J. Atmos. Sci.*,
677 **56**, 4050–4058.
- 678 29. Mapes, B. E., 1993: Gregarious Tropical Convection. *J. Atmos. Sci.*, **50**, 2026–2037.
- 679 30. Mapes, B. E., 2000: Convective inhibition, subgrid-scale triggering energy, and
680 stratiform instability in a toy tropical wave model. *J. Atmos. Sci.*, **57**, 1515–1535.
- 681 31. Nesbitt, S. W., E. J. Zipser, and D. J. Cecil, 2000: A census of precipitation features
682 in the tropics using TRMM: Radar, ice scattering, and lightning observations. *J.*
683 *Climate*, **13**, 4087–4106.
- 684 32. Nicholls, M. E., R. A. Pielke, and W. R. Cotton, 1991: Thermally Forced Gravity
685 Waves in an Atmosphere at Rest. *J. Atmos. Sci.*, **48**, 1869–1884.
- 686 33. Nicholls, M. E., and M. Montgomery, 2013: An examination of two pathways to
687 tropical cyclogenesis occurring in idealized simulations with a cloud-resolving
688 numerical model. *Atmos. Chem. Phys.*, **13**, 5999–6022.
- 689 34. Nicholls, M. E., 2015: An investigation of how radiation may cause accelerated
690 rates of tropical cyclogenesis and diurnal cycles of convective activity. *Atmos.*
691 *Chem. Phys.*, **15**, 9003–9029.
- 692 35. Nolan, D. S., 2007: What is the trigger for tropical cyclogenesis? *Aust. Meteor. Mag.*,
693 **56**, 241–266.
- 694 36. Skamarock, W. C., Klemp, J. B., Dudhia, J., Gill, D. O., Liu, Z., Berner, J., Wang,
695 W., Powers, J. G., Duda, M. G., Barker, D. M., and Huang, X.-Y. (2019), A
696 Description of the Advanced Research WRF Model Version 4, UCAR/NCAR,
697 <https://doi.org/10.5065/1DFH-6P97>.
- 698 37. Takayabu, Y. N., 1994: Large-scale cloud disturbances associated with equa torial
699 waves. Part II: Westward-propagating inertio-gravity waves. *J. Meteor. Soc. Japan*,
700 **72**, 451–465.
- 701 38. Takayabu, Y. N., K. M. Lau, and C. H. Sui, 1996: Observation of a quasi-2-day

702 wave during TOGA COARE. *Mon. Wea. Rev.*, **124**, 1892–1913.

703 39. Thompson, G., R. M. Rasmussen, and K. Manning, 2004: Explicit forecasts of
704 winter precipitation using an improved bulk microphysics scheme. Part I:
705 Description and sensitivity analysis. *Mon. Wea. Rev.*, **132**, 519–542.

706 40. Tulich, S. N., and B. E. Mapes, 2010: Transient environmental sensitivities of
707 explicitly simulated tropical convection. *J. Atmos. Sci.*, **67**, 923–940.

708 41. Wheeler, M., and G. N. Kiladis, and P. J. Webster, 2000: Large-scale dynamical
709 fields associated with convectively coupled equatorial waves. *J. Atmos. Sci.*, **57**,
710 613–639.

711 42. Wu, Q., Ruan, Z., Chen, D. and Lian, T., 2015: Diurnal variations of tropical
712 cyclone precipitation in the inner and outer rainbands. *J. Geophys. Res.*, **120**, 1–11.

713 43. Wu, Z., E. S. Sarachik, and D. S. Battisti, 2000b: Vertical structure of convective
714 heating and the three-dimensional structure of the forced circulation on an
715 equatorial beta plane. *J. Atmos. Sci.*, **57**, 2169–2187.

716 44. Wu, Z., 2003: A shallow CISK, deep equilibrium mechanism for the interaction
717 between large-scale convection and large-scale circulations in the tropics. *J. Atmos.*
718 *Sci.*, **60**, 377–392.

719 45. Yang, B., and Z.-M. Tan, 2020: Interactive radiation accelerates the intensification
720 of the midlevel vortex for tropical cyclogenesis. *J. Atmos. Sci.*, **77**, 4051–4065.

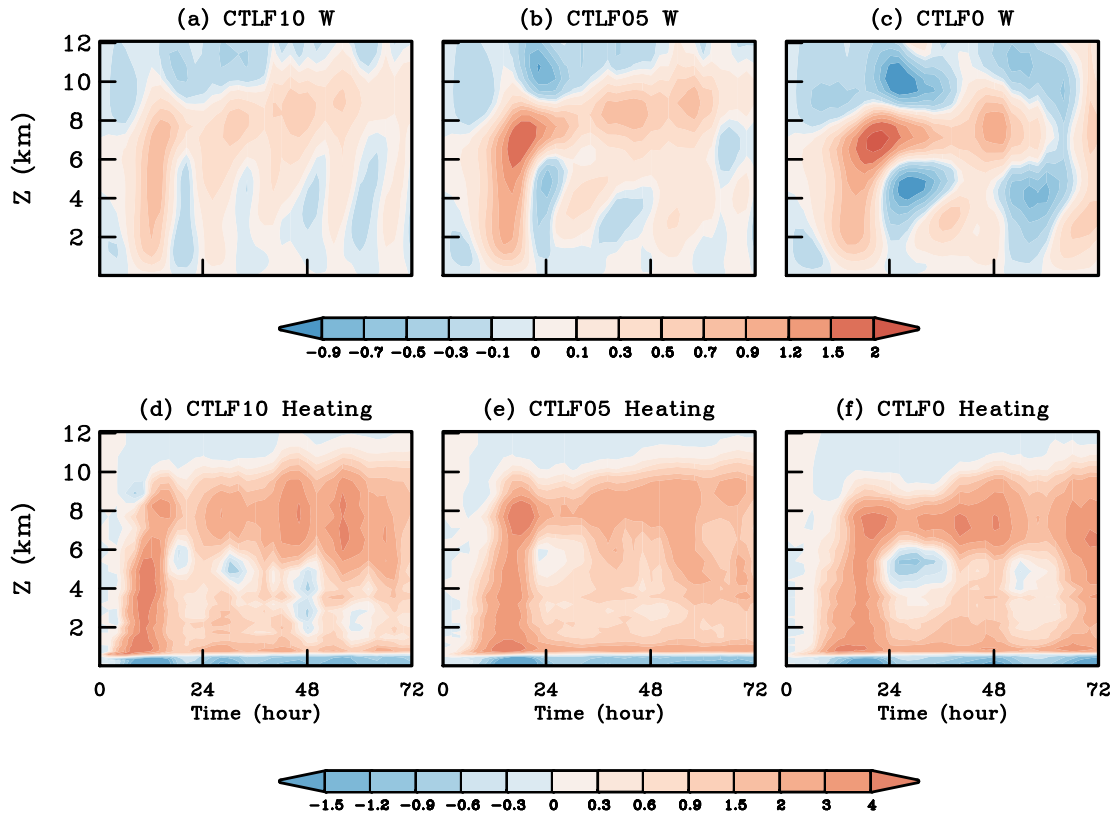
721

722

723

724
725
726

Appendix



727
728
729
730
731

Fig. S1 Time-height plot of (a) vertical velocity (cm s^{-1}) and (d) diabatic heating (K day^{-1}), all averaged in the inner 150 km radii of the domain in CTLF10. (b), (e) and (c), (f) are for CTLF05 and CTLF0, respectively.